Journal of Global Positioning Systems (2023)
Vol. 19, Joint No. 1 & No. 2: 79-98
DOI:10.5081/jgps.19.1.79

Three Attitude Models and their Characterization in the Generic Multisensor Integration Strategy for Kinematic Positioning and Navigation

Benjamin Brunson* and Jianguo Wang
Department of Earth and Space Science and Engineering
Lassonde School of Engineering, York University, Toronto, Canada
Emails: brunson@yorku.ca and jgwang@yorku.ca
* Corresponding Author

Abstract: This research aims at further completing our novel Generic Multisensor Integration Strategy (GMIS) with the systematic development of three alternate attitude models, i.e., roll-pitch-heading (RPH), direction cosine matrix (DCM), and quaternion. The GMIS' potential for a true sensor level data fusion is leveraged to its full extent here by facilitating comprehensive error analysis framework in Kalman filtering. A comparative analysis between the solutions resulted from the GMIS associated with each attitude model have been analysed and compared through real road test data. The attitude models were found to perform very consistently, exhibiting the same behaviours in the residuals of the process noise and measurement vectors along with the estimated variance components. Besides, an analysis was conducted to investigate how each attitude model reacts to a sudden trajectory variation captured by the IMU. Each attitude model still performed consistently, but the DCM model in particular exhibited resistance to absorbing erroneous observations into its process noise estimates.

KEY WORDS: **G**eneric **M**ultisensor Integration Strategy, Attitude models**,** IMU Measurement Model, Double-Differenced GNSS, Kalman Filter with Constraints, Error Analysis, **V**ariance Component Estimation.

1. INTRODUCTION

The naturalization of GNSS-aided Inertial Navigation from the military industry into Surveying and Mapping defines one of the most successful technological evolutions in Spatial Science and Engineering over the past several decades. Specifically, it spawned the so-called Direct-Georeferencing Technology, which is defined as the process of assigning the Exterior Orientation of each image frame or scan line directly, without the need to use traditional aerial triangulation techniques [Hutton and Mostafa, 2005; Dreier et al, 2021]. The use of this technology has been widely adopted across many applications, ranging from surveying to kinematic positioning/navigation for airborne, marine and land robotic/unmanned vehicles at positioning accuracies even approaching the cm level. Meanwhile, an increasing number of low-cost positioning and orientation sensors have been being made available on the market such as MEMS IMUs, GNSS receivers, cameras and LiDAR. This continually drives more advanced research and development activities in academia and industry.

One important area of research is to innovate the multisensor integration strategy, or data fusion strategy, as the traditional IMU-centered integration strategy does not take advantage of modern advancements in computers, sensors, and data science. A central component of the traditional integration strategy, e.g. with integrating IMU, GNSS receivers, odometers, etc., is to assign the IMU sensor as the core sensor while all others are used as aiding sensors. Once the measurements from any aiding sensors become available, error measurements are generated as the differences between them and the derived values of the same types of the measurements from the inertial dead reckoning solutions based on the IMU output. Then, the error measurements are used to conduct the measurement update in the navigation Kalman filter. In this paradigm, the multisensor data fusion is not possible at the sensor level in terms of how to utilize the measurements, and the measurement update rate of the Kalman Filter (KF) depends upon the data rates of the aiding sensors, typically operating at a much lower frequency than the IMU data rate. Moreover, the information in IMU measurements could be used

Editor-In-Charge: Dr. Qian Sun

multiple times in one estimation process in the event of multiple integrated aiding sensors. The IMU output is not directly used to conduct the measurement updates in the navigation KF. In this way, the free inertial navigation calculation between two observation epochs of an aiding sensor (e.g. GNSS) could suffer from significant drifting, especially while working with low-cost IMUs and/or during the aiding sensor data gaps [Wang et al, 2015; Qian et al, 2015; Qian, 2017]. Unfortunately, the majority of current research and development in multisensor integrated kinematic positioning/navigation systems simply build on top of the existing integration strategy, likely due to it being broadly accepted in the field [Farrell, 1995; Wagner and Wieneke, 2003].

The Generic Multisensor Integration Strategy (GMIS) [Qian, 2017; Qian et al, 2015, 2016; Wang et al, 2015; Wang and Sternberg, 2000; Wang, 1997] models the basic kinematic states such the position, velocity and acceleration vectors associated with the attitude angles on the ground of 3D kinematics, which allows directly applying the measurements from each of the sensors feasibly through measurement updates in Kalman filtering so that their individual error behaviours could be directly studied, including the gyroscopes and accelerometers. Such studies are not possible from IMU/GNSS error measurements under the traditional integration strategy. The GMIS is also unique in that it decouples the system model from the IMU measurements, which allows for more intuitive performance analysis of both measurement residuals and kinematic model (through the residuals of the process noise vector). A workflow diagram of the GMIS for a single IMU and two GNSS sensors (using double-differenced GNSS observations) is illustrated in Fig. 1.1. It may be readily expanded to accommodate any number/configuration of positioning/attitude sensors, which is another benefit to using the GMIS. However, no intensive study of attitude models under the GMIS has been conducted yet, which has motivated this research specifically.

Undoubtedly, attitude estimation is an essential part of any integrated inertial navigation system, so this work aims at further completing our GMIS with systematically studying three alternate attitude models, i.e., roll-pitch-heading (RPH), direction cosine matrix (DCM), and quaternion within the scope of the GMIS.

The most common and direct way to represent system attitude in 3D kinematics is using the roll-pitch-heading angles, but this attitude model famously suffers from the Gimbal Lock phenomenon when its pitch is approaching ±90 degrees in inertial dead reckoning. As a result, one may adopt alternative attitude models that do not suffer from Gimbal Lock, including: the Direction Cosine Matrix (DCM) representation [Choukroun et al, 2010; Wang and Rajamani, 2018], the axis-angle representation [Özgür Doruk, 2009; Meng et al, 2010], and the quaternion representation [Zhu et al, 2021; Yang, 2012; Sabatini, 2006]. There is a significant body of research exploring the efficiency of these alternative attitude models within the scope of traditional IMU-centered multisensor integrated navigation systems [e.g. Fresk and Nikolakopoulos, 2013; Song et al, 2020], but there is comparatively little detailing the accuracy impact of changing the attitude model as well as its associated full-scale system model. The literature that does focus on comparing the accuracy of different attitude models relies on either the availability of an established ground truth trajectory or using simulated data [Prasetyo and Musa, 2021; Sheng and Zhang, 2015; Golabek et al, 2022]. Indeed, it is difficult to directly compare their accuracies without converting between attitude representations.

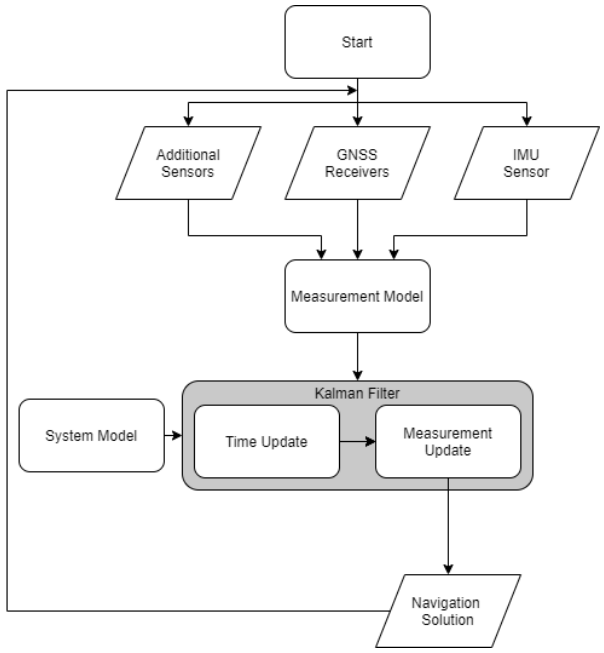

Fig. 1.1 Flowchart of the general workflow of integrating positioning sensors in the GMIS.

As a competent analytical tool in discrete Kalman filtering, a framework for comprehensive error analysis [Wang, 1997, 2008, 2009; Caspary and Wang, 1998; Wang et al, 2021] has been developed and also further extended to the state-constrained Kalman Filter [Wang et al, 2022] that allows for the calculation of additional quantities, which could be used to directly compare between attitude models using a comprehensive error analysis accounting for the following:

- Residual estimates for the observation and process noise vectors;
- Redundancy contributions of the observation and process noise vectors; and
- Variance factors for each element in the observation and process noise vectors.

These quantities provide significant insight into the accuracy of the position/attitude estimation process without requiring the use of a ground truth trajectory. Additionally, the estimated variance factors for the process noise vector and different types of the sensor measurements are unitless, which allows for direct performance comparison between different attitude models without requiring a conversion between attitude representations.

This research is to clearly present the analytical algorithms of the three attitude models in the GMIS. Combining the detailed information obtainable from the GMIS and the comprehensive error analysis enabled for the rigorous system state-constrained extended KF (EKF), this paper conducts a comprehensive analysis of the performance of each attitude model.

Following this introduction, Section 2 details the formulation of each attitude model in the GMIS, including a description of the matrix partitioning used in formulating the positioning KF and constraints required under each attitude model. Section 3 describes the system state-constrained KF and the quantities that are used for comprehensive error analysis. Section 4 then conducts a comparative analysis between each of the different attitude models, with a particular focus on comparing their time-varying variance factors.

2. MODELING IMU MEASUREMENTS IN THE GMIS

2.1 Partitioning the EKF Matrices

Generally, a KF uses a system model to define system kinematics, and measurement models to define how any observations relate to the current system state vector. At time t_{k+1}, these models are defined to be

$$\boldsymbol{x}(k+1) = \boldsymbol{A}(k+1,k)\boldsymbol{x}(k) + \boldsymbol{B}(k+1,k)\boldsymbol{w}(k) \quad (2.1)$$

$$\boldsymbol{z}(k+1) = \boldsymbol{C}(k+1)\boldsymbol{x}(k+1) + \boldsymbol{\Delta}(k+1) \quad (2.2)$$

wherein $\boldsymbol{x}(k+1)$ is the system state vector, $\boldsymbol{A}$ is the transition matrix that defines the system kinematic models from t_k to t_{k+1}, $\boldsymbol{w}$ is the process noise vector that defines the errors in those kinematic models, $\boldsymbol{B}$ represents the process noise transition matrix, $\boldsymbol{z}$ is the observation vector, $\boldsymbol{C}$ is the design matrix, and $\boldsymbol{\Delta}$ is the measurement noise vector.

Additionally, constraint equations may be imposed upon the system state elements using

$$\boldsymbol{H}(\boldsymbol{x}(k+1), k+1) + \boldsymbol{h}(k+1) = o \quad (2.3)$$

where $\boldsymbol{H}$ is the set of constraint equations imposed on the system state, and $\boldsymbol{h}$ is a vector of constants defined by the constraint equations.

In the navigation KF used in the GMIS, the basic system state vector consists of the linear position, velocity, and acceleration of the system, as well any attitude parameters and their first order time-derivatives. Generally, the system model is realized after kinematics that govern the motion of a moving system platform. For example, the linear motion of the system may be represented using an assumed constant linear acceleration between observation epochs, and the angular motion of the system may be represented using an assumed constant angular velocity between observation epochs.

To accommodate multiple attitude models and observations from multiple sources, it is useful to partition the states and their associated transition and design matrices to allow for their modular construction in software implementation. The state vector may be partitioned into groups:

- Position, velocity and acceleration;
- Attitude and angular velocity;
- GNSS integer ambiguity parameters; and
- IMU systematic error states (gyro/accelerometer bias and scale factor errors).

This partitioned state vector is expressed as

$$\boldsymbol{x} = \begin{bmatrix} \boldsymbol{x}_p^T & \boldsymbol{x}_a^T & \boldsymbol{x}_\lambda^T & \boldsymbol{x}_{IMU}^T \end{bmatrix}^T \quad (2.4)$$

wherein the subscripts p, a, λ, and imu stand for the linear kinematic state (position, velocity, and acceleration) vector, the angular state (attitude and angular velocity) vector, the GNSS ambiguity vector, and the IMU systematic error vector, respectively. Correspondingly, the transition matrix, process noise vector, and process noise transition matrix given in (2.1) are partitioned as follows

$$\mathbf{A} = \begin{bmatrix} \mathbf{A}_p & \mathbf{0} & \mathbf{0} & \mathbf{0} \\ \mathbf{0} & \mathbf{A}_a & \mathbf{0} & \mathbf{0} \\ \mathbf{0} & \mathbf{0} & \mathbf{A}_\lambda & \mathbf{0} \\ \mathbf{0} & \mathbf{0} & \mathbf{0} & \mathbf{A}_{IMU} \end{bmatrix} \quad (2.5)$$

$$\boldsymbol{w} = \begin{bmatrix} \boldsymbol{w}_p^T & \boldsymbol{w}_a^T & \boldsymbol{w}_\lambda^T & \boldsymbol{w}_{IMU}^T \end{bmatrix}^T \quad (2.6)$$

$$\mathbf{B} = \begin{bmatrix} \mathbf{B}_p & \mathbf{0} & \mathbf{0} & \mathbf{0} \\ \mathbf{0} & \mathbf{B}_a & \mathbf{0} & \mathbf{0} \\ \mathbf{0} & \mathbf{0} & \mathbf{B}_\lambda & \mathbf{0} \\ \mathbf{0} & \mathbf{0} & \mathbf{0} & \mathbf{B}_{IMU} \end{bmatrix} \quad (2.7)$$

For the GNSS/IMU integrated system with which this work proceeds, there are three constituent sources of raw measurements:

- The double-differenced L1 C/A and L1/L2 carrier phase observations from a pair of GPS receivers for relative positioning (one static reference and one rover);

- Specific force observations from three accelerometers in a strapdown IMU; and
- Angular rate observations from three gyroscopes in a strapdown IMU.

Further, the system innovation vector is partitioned into three subvectors

$$\boldsymbol{d} = \begin{bmatrix} \boldsymbol{d}_g^T & \boldsymbol{d}_s^T & \boldsymbol{d}_G^T \end{bmatrix}^T \tag{2.8}$$

where $\boldsymbol{d}_g$, $\boldsymbol{d}_s$, and $\boldsymbol{d}_G$ correspond to the gyroscope, accelerometer, and GNSS observables at t_{k+1}, respectively.

The design matrix is partitioned so as to separate the partitioned system state elements and to separate the observation types, as

$$\boldsymbol{C} = \begin{bmatrix} \boldsymbol{C}_{g,p} & \boldsymbol{C}_{g,a} & \boldsymbol{C}_{g,\lambda} & \boldsymbol{C}_{g,IMU} \\ \boldsymbol{C}_{s,p} & \boldsymbol{C}_{s,a} & \boldsymbol{C}_{s,\lambda} & \boldsymbol{C}_{s,IMU} \\ \boldsymbol{C}_{G,p} & \boldsymbol{C}_{G,a} & \boldsymbol{C}_{G,\lambda} & \boldsymbol{C}_{G,IMU} \end{bmatrix} \tag{2.9}$$

This partitioning allows for a finer identification of what quantities change or remain the same between different attitude models. Only $\boldsymbol{x}_a$ has a different definition when changing the attitude model, so only $\boldsymbol{C}_{g,a}$, $\boldsymbol{C}_{s,a}$, and $\boldsymbol{C}_{G,a}$ will potentially need to be redefined when changing the attitude model.

2.2 Position System Model in the GMIS

Regardless of the attitude model being used, the system model defining how the position changes through time should be consistent. For this research, we use a constant linear acceleration model as the system model for the change in linear position. This can be expressed as

$$\boldsymbol{x}_p(k+1) = \begin{bmatrix} \boldsymbol{I}_3 & \Delta t_{k+1}\boldsymbol{I}_3 & \frac{1}{2}\Delta t_{k+1}\boldsymbol{I}_3 \\ \boldsymbol{0}_3 & \boldsymbol{I}_3 & \Delta t_{k+1}\boldsymbol{I}_3 \\ \boldsymbol{0}_3 & \boldsymbol{0}_3 & \boldsymbol{I}_3 \end{bmatrix} \boldsymbol{x}_p(k) + \begin{bmatrix} \frac{1}{6}\Delta t_{k+1}^3\boldsymbol{I}_3 \\ \frac{1}{2}\Delta t_{k+1}^2\boldsymbol{I}_3 \\ \Delta t_{k+1}\boldsymbol{I}_3 \end{bmatrix} \dot{\boldsymbol{a}}(k) = \boldsymbol{A}_p\boldsymbol{x}_p(k) + \boldsymbol{B}_p\dot{\boldsymbol{a}}(k) \tag{2.10}$$

where $\dot{\boldsymbol{a}}(k)$ is the third-order motion process noise vector, or system jerk vector, expressed in the local ENU navigation frame. Modeling linear system motion in this frame ensures that its system model remains unaffected by the choice of attitude model.

2.3 IMU Observation Equations

Before detailing the attitude model-specific IMU observation equations, it is important to establish the general IMU observation equations that will be adapted to each attitude model. In general, the gyroscope observations are modeled as

$$\begin{aligned} \boldsymbol{\omega}_{ib}^b &= \boldsymbol{\omega}_{nb}^b - \boldsymbol{b}_g - \boldsymbol{S}_g\boldsymbol{\omega}_{ib,meas}^b \\ &\quad + \boldsymbol{C}_n^b(\boldsymbol{\omega}_{ie}^n + \boldsymbol{\omega}_{en}^n) + \Delta_{\boldsymbol{\omega}_{ib}^b} \end{aligned} \tag{2.11}$$

where $\boldsymbol{\omega}_{ib}^b$ denotes the gyro measurement vector of the angular rates of the body frame with respect to the inertial frame in the body frame, $\boldsymbol{b}_g$ denotes the gyroscope bias vector, $\boldsymbol{S}_g$ denotes the gyroscope scale factor error matrix, which is diagonal when not considering cross-coupling errors, $\boldsymbol{C}_n^b$ denotes the three-dimensional rotation matrix from the navigation frame to the body frame (note: do not confuse this with the design matrix $\boldsymbol{C}$ in (2.2) and (2.9)), $\boldsymbol{\omega}_{ie}^n$ denotes the angular velocity of Earth with respect to the inertial frame, expressed in the navigation frame, $\boldsymbol{\omega}_{en}^n$ denotes the angular velocity of the navigation frame with respect to Earth in the navigation frame, and $\Delta_{\boldsymbol{\omega}_{ib}^b}$ is the noise vector.

In general, the accelerometer specific force observations at t_{k+1} are modeled as

$$\begin{aligned} \boldsymbol{f}_{ib}^b &= \boldsymbol{C}_n^b\boldsymbol{a} + \boldsymbol{C}_n^b\boldsymbol{g} - \boldsymbol{b}_a - \boldsymbol{S}_a\boldsymbol{f}_{ib}^b + \boldsymbol{C}_n^b\{2\boldsymbol{\omega}_{ie}^n + \boldsymbol{\omega}_{en}^n\} \times \boldsymbol{v} + \boldsymbol{C}_n^b\boldsymbol{\omega}_{ib}^b \times \boldsymbol{\omega}_{ib}^b \times \boldsymbol{r} \\ &= \boldsymbol{C}_n^b\boldsymbol{s} - \boldsymbol{b}_a - \boldsymbol{S}_a\boldsymbol{f}_{ib,meas}^b + \Delta_{\boldsymbol{f}_{ib}^b} \end{aligned} \tag{2.12}$$

where $\boldsymbol{f}_{ib}^b$ denotes the specific force of the body frame with respect to the inertial frame, expressed in the body frame, $\boldsymbol{a}$ denotes the acceleration of the body frame at t_{k+1}, expressed in the navigation frame, $\boldsymbol{g}$ denotes the local gravity vector, expressed in the navigation frame; $\boldsymbol{v}$ denotes the velocity of the body frame, expressed in the navigation frame, $\boldsymbol{r}$ denotes the lever arm vector for the IMU sensor in the body frame, $\Delta_{\boldsymbol{f}_{ib}^b}$ is the noise vector, and $\boldsymbol{s}$ is a helping parameter vector used in collecting like terms for $\boldsymbol{C}_n^b$, which is used in the subsequent sections.

In both (2.11) and (2.12), $\boldsymbol{C}_n^b$ and $\boldsymbol{\omega}_{nb}^b$ are not specific to any particular attitude representation, but could be calculated from the defining parameters of any attitude model. These equations therefore form the basis of the IMU observation models regardless of how the attitude is modeled.

3. ATTITUDE MODELS IN THE GMIS

3.1 Roll-Pitch-Heading Formulation

The roll-pitch-heading angles are three primitive parameters that uniquely represent the attitude of an object in 3D space. There are multiple equivalent ways to construct the attitude matrix from these angles. For instance, the attitude matrix from the navigation to the body frame used in this research is given as follows

$$\boldsymbol{C_n^b} = \boldsymbol{R_2}(\alpha)\boldsymbol{R_1}(\beta)\boldsymbol{R_3}(\gamma) \tag{3.1}$$

where α, β, and γ are the system roll, pitch, and heading, respectively. The system's angular velocities defined by their 1st order time derivatives ($\dot{\alpha}$, $\dot{\beta}$, $\dot{\gamma}$) are included in the system state vector so that one has

$$\boldsymbol{x_a} = [\alpha \quad \beta \quad \gamma \quad \dot{\alpha} \quad \dot{\beta} \quad \dot{\gamma}] \tag{3.2}$$

Under consideration that the attitude angles vary linearly with time, their second order time-derivatives ($\ddot{\alpha}$, $\ddot{\beta}$, $\ddot{\gamma}$) define their associated process noise. The system model governing the attitude is therefore given as follows

$$\alpha(k+1) = \alpha(k) + \dot{\alpha}(k)\Delta t_{k+1} + \frac{1}{2}\ddot{\alpha}(k)\Delta t_{k+1}^2 \tag{3.3}$$

$$\beta(k+1) = \beta(k) + \dot{\beta}(k)\Delta t_{k+1} + \frac{1}{2}\ddot{\beta}(k)\Delta t_{k+1}^2 \tag{3.4}$$

$$\gamma(k+1) = \gamma(k) + \dot{\gamma}(k)\Delta t_{k+1} + \frac{1}{2}\ddot{\gamma}(k)\Delta t_{k+1}^2 \tag{3.5}$$

with $\Delta t_{k+1} = t_{k+1} - t_k$, the associated transition matrix of

$$\mathbf{A}_a = \begin{bmatrix} \boldsymbol{I_3} & \Delta t_{k+1}\boldsymbol{I_3} \\ \boldsymbol{0_3} & \boldsymbol{I_3} \end{bmatrix} \tag{3.6}$$

and the process noise transition matrix of

$$\mathbf{B}_a = \begin{bmatrix} \frac{1}{2}\Delta t_{k+1}^2\boldsymbol{I_3} \\ \Delta t_{k+1}\boldsymbol{I_3} \end{bmatrix} \tag{3.7}$$

After [Zhao, 2016], the differential equation relating $\boldsymbol{\omega_{nb}^b}$ and ($\dot{\alpha}$, $\dot{\beta}$, $\dot{\gamma}$) is given as

$$\boldsymbol{\omega_{nb}^b} = \begin{bmatrix} 0 & \cos\alpha & \sin\alpha\cos\beta \\ 1 & -\sin\beta & 0 \\ 0 & \sin\alpha & -\cos\alpha\cos\beta \end{bmatrix} \begin{bmatrix} \dot{\alpha} \\ \dot{\beta} \\ \dot{\gamma} \end{bmatrix} \tag{3.8}$$

The substitution of (3.8) into (2.11) results in the following submatrix

$$\boldsymbol{C_{g,a}} = \begin{bmatrix} & 0 & \cos\alpha & \sin\alpha\cos\beta \\ \boldsymbol{0_3} & 1 & -\sin\beta & 0 \\ & 0 & \sin\alpha & -\cos\alpha\cos\beta \end{bmatrix} \tag{3.9}$$

It is hereby worth noting that the application of (3.8) in (3.9) and (2.11) is not possible for the singularity when $\beta = \pm 90°$, whereas such singularity is inseparable from the inertial measurements-based free dead reckoning calculation.

The accelerometer observation equation remains unchanged when using the roll-pitch-heading attitude model, but has a modified design matrix of

$$\boldsymbol{C_{s,a}} = \left[\frac{\partial \boldsymbol{R_2}(\alpha)}{\partial \alpha}\boldsymbol{R_1}(\beta)\boldsymbol{R_3}(\gamma)\boldsymbol{s} \quad \boldsymbol{R_2}(\alpha)\frac{\partial \boldsymbol{R_1}(\beta)}{\partial \beta}\boldsymbol{R_3}(\gamma)\boldsymbol{s} \quad \boldsymbol{R_1}(\alpha)\boldsymbol{R_2}(\beta)\frac{\partial \boldsymbol{R_3}(\gamma)}{\partial \gamma}\boldsymbol{s} \quad \boldsymbol{0_3}\right] \tag{3.10}$$

3.2 Direction Cosine Matrix Formulation

3.2.1 The DCM States

In the DCM representation, the individual elements of the attitude matrix are each considered states and their first order time-derivatives are used to model their changes. This results in a total of 18 DCM states. Specifically, the rotation matrix from the navigation frame to the body frame is given in elements as follows

$$\boldsymbol{C_n^b} = \begin{bmatrix} c_{11} & c_{12} & c_{13} \\ c_{21} & c_{22} & c_{23} \\ c_{31} & c_{32} & c_{33} \end{bmatrix} \tag{3.11}$$

The portion of the system state vector that defines the attitude parameters may be expressed as

$$\boldsymbol{x_a} = [\boldsymbol{C_1} \quad \boldsymbol{C_2} \quad \boldsymbol{C_3} \quad \dot{\boldsymbol{C}}_1 \quad \dot{\boldsymbol{C}}_2 \quad \dot{\boldsymbol{C}}_3]^T \tag{3.12}$$

where $\boldsymbol{C_i} = [c_{i1} \quad c_{i2} \quad c_{i3}]$ and $\dot{\boldsymbol{C}}_i = [\dot{c}_{i1} \quad \dot{c}_{i2} \quad \dot{c}_{i3}]$ for i = 1, 2, 3.

The DCM states are considered to change linearly with time, with their second order time-derivatives defining the associated process noise. The kinematic model governing this attitude model is therefore given by the nine system equations

$$c_{ij}(k+1) = c_{ij}(k) + \dot{c}_{ij}(k)\Delta t_{k+1} + \frac{1}{2}\ddot{c}(k)\Delta t_{k+1}^2, i \in (1,2,3), j \in (1,2,3) \tag{3.13}$$

with the associated transition matrix of

$$\mathbf{A}_a \begin{bmatrix} \boldsymbol{I_9} & \Delta t_{k+1}\boldsymbol{I_9} \\ \boldsymbol{0_9} & \boldsymbol{I_9} \end{bmatrix} \tag{3.14}$$

and the process noise transition matrix of

$$\mathbf{B}_a = \begin{bmatrix} \frac{1}{2}\Delta t_{k+1}^2\boldsymbol{I_9} \\ \Delta t_{k+1}\boldsymbol{I_9} \end{bmatrix} \tag{3.15}$$

The attitude parameters may be connected to $\boldsymbol{\omega_{nb}^b}$ via the Poisson equation [Salychev, 1998]

$$\dot{\boldsymbol{C}}_{\boldsymbol{n}}^{\boldsymbol{b}} = \boldsymbol{C}_{\boldsymbol{n}}^{\boldsymbol{b}}[\boldsymbol{\omega}_{\boldsymbol{nb}}^{\boldsymbol{b}} \times] \tag{3.16}$$

where $[\boldsymbol{v} \times]$ denotes the skew-symmetric cross product matrix of a vector $\boldsymbol{v}$. (3.16) can be rearranged to isolate $\boldsymbol{\omega}_{\boldsymbol{nb}}^{\boldsymbol{b}}$

$$[\boldsymbol{\omega}_{\boldsymbol{nb}}^{\boldsymbol{b}} \times] = \left(\boldsymbol{C}_{\boldsymbol{n}}^{\boldsymbol{b}}\right)^T \dot{\boldsymbol{C}}_{\boldsymbol{n}}^{\boldsymbol{b}} \tag{3.17}$$

which yields $\boldsymbol{\omega}_{\boldsymbol{nb}}^{\boldsymbol{b}}$ in components as

$$\boldsymbol{\omega}_{\boldsymbol{nb}}^{\boldsymbol{b}} = \begin{bmatrix} C_{13}\dot{C}_{12} + C_{23}\dot{C}_{22} + C_{33}\dot{C}_{32} \\ C_{11}\dot{C}_{13} + C_{21}\dot{C}_{23} + C_{31}\dot{C}_{33} \\ C_{12}\dot{C}_{11} + C_{22}\dot{C}_{21} + C_{32}\dot{C}_{31} \end{bmatrix} \tag{3.18}$$

which can directly be used in (2.11).

The corresponding portion of the design matrix may then be redefined to be

$$\boldsymbol{C}_{g,a} = \begin{bmatrix} 0 & 0 & \dot{c}_{12} & 0 & 0 & \dot{c}_{22} & 0 & 0 & \dot{c}_{32} & 0 & c_{13} & 0 & 0 & c_{23} & 0 & 0 & c_{33} & 0 \\ \dot{c}_{13} & 0 & 0 & \dot{c}_{23} & 0 & 0 & \dot{c}_{33} & 0 & 0 & 0 & 0 & c_{11} & 0 & 0 & c_{21} & 0 & 0 & c_{31} \\ 0 & \dot{c}_{11} & 0 & 0 & \dot{c}_{21} & 0 & 0 & \dot{c}_{31} & 0 & c_{12} & 0 & 0 & c_{22} & 0 & 0 & c_{32} & 0 & 0 \end{bmatrix} \tag{3.19}$$

The accelerometer observation equations remain unchanged when using the DCM attitude model, but the redefinition of the rotation matrix leads the attitude portion of the design matrix to be redefined as

$$\boldsymbol{C}_{\boldsymbol{s},\boldsymbol{a}} = \begin{bmatrix} \boldsymbol{s}^T & \boldsymbol{0}_{1,3} & \boldsymbol{0}_{1,3} & \boldsymbol{0}_{1,9} \\ \boldsymbol{0}_{1,3} & \boldsymbol{s}^T & \boldsymbol{0}_{1,3} & \boldsymbol{0}_{1,9} \\ \boldsymbol{0}_{1,3} & \boldsymbol{0}_{1,3} & \boldsymbol{s}^T & \boldsymbol{0}_{1,9} \end{bmatrix} \tag{3.20}$$

3.2.2 DCM State Constraints

The attitude of a system in 3D space is sufficiently described using 3 functionally independent parameters, and the change of a system's attitude is similarly described using 3 functionally independent parameters. This means 12 of the 18 chosen DCM states are redundant. This necessitates the inclusion of 12 constraints on the DCM attitude states to avoid over-parameterization.

The first six equations are readily derived from the orthogonal property of an attitude matrix

$$\begin{bmatrix} \boldsymbol{C}_1 \\ \boldsymbol{C}_2 \\ \boldsymbol{C}_3 \end{bmatrix} [\boldsymbol{C}_1^T \quad \boldsymbol{C}_2^T \quad \boldsymbol{C}_3^T] = \boldsymbol{I}_3 \tag{3.21}$$

of which the upper or lower triangular elements of the identity matrix in (3.21) leads to the six constraints:

$$\boldsymbol{C}_1\boldsymbol{C}_1^T = 1 \tag{3.22}$$

$$\boldsymbol{C}_2\boldsymbol{C}_2^T = 1 \tag{3.23}$$

$$\boldsymbol{C}_3\boldsymbol{C}_3^T = 1 \tag{3.24}$$

$$\boldsymbol{C}_1\boldsymbol{C}_2^T = 0 \tag{3.25}$$

$$\boldsymbol{C}_1\boldsymbol{C}_3^T = 0 \tag{3.26}$$

$$\boldsymbol{C}_2\boldsymbol{C}_3^T = 0 \tag{3.27}$$

Similarly, dealing with the 6 remaining redundant states among the 9 time-derivatives of the DCM states further requires the construction of 6 additional constraints. There are two strategies to defining these additional constraints:

1) Enforcing that the matrix product in the rearranged Poisson Equation in (3.17) is a skew-symmetric matrix (i.e. diagonal elements should be 0 and the sum of an off-diagonal element with its transpose should be 0); or
2) Using the time-derivatives of the constraint equations from (3.22) to (3.27).

It can be proven that no matter which strategy is used, the same six additional constraints are derived:

$$\boldsymbol{C}_1\dot{\boldsymbol{C}}_1^T = 0 \tag{3.28}$$

$$\boldsymbol{C}_2\dot{\boldsymbol{C}}_2^T = 0 \tag{3.29}$$

$$\boldsymbol{C}_3\dot{\boldsymbol{C}}_3^T = 0 \tag{3.30}$$

$$\boldsymbol{C}_1\dot{\boldsymbol{C}}_2^T + \dot{\boldsymbol{C}}_1\boldsymbol{C}_2^T = 0 \tag{3.31}$$

$$\boldsymbol{C}_1\dot{\boldsymbol{C}}_3^T + \dot{\boldsymbol{C}}_1\boldsymbol{C}_3^T = 0 \tag{3.32}$$

$$\boldsymbol{C}_2\dot{\boldsymbol{C}}_3^T + \dot{\boldsymbol{C}}_2\boldsymbol{C}_3^T = 0 \tag{3.33}$$

Together, the 12 constraints from (3.22) to (3.33) are necessary to eliminate the functional singularity due to the use of 12 redundant DCM states. As all the constraint equations are non-linear, their linearized coefficient matrix (i.e. the partial derivatives of the constraint equations with respect to the state elements) is estimated as

$$\boldsymbol{H}_{\boldsymbol{DCM},\boldsymbol{a}} = \begin{bmatrix} 2\boldsymbol{C}_1 & \boldsymbol{0} & \boldsymbol{0} & \boldsymbol{0} & \boldsymbol{0} & \boldsymbol{0} \\ \boldsymbol{0} & 2\boldsymbol{C}_2 & \boldsymbol{0} & \boldsymbol{0} & \boldsymbol{0} & \boldsymbol{0} \\ \boldsymbol{0} & \boldsymbol{0} & 2\boldsymbol{C}_3 & \boldsymbol{0} & \boldsymbol{0} & \boldsymbol{0} \\ \boldsymbol{C}_2 & \boldsymbol{C}_1 & \boldsymbol{0} & \boldsymbol{0} & \boldsymbol{0} & \boldsymbol{0} \\ \boldsymbol{C}_3 & \boldsymbol{0} & \boldsymbol{C}_1 & \boldsymbol{0} & \boldsymbol{0} & \boldsymbol{0} \\ \boldsymbol{0} & \boldsymbol{C}_3 & \boldsymbol{C}_2 & \boldsymbol{0} & \boldsymbol{0} & \boldsymbol{0} \\ \dot{\boldsymbol{C}}_1 & \boldsymbol{0} & \boldsymbol{0} & \boldsymbol{C}_1 & \boldsymbol{0} & \boldsymbol{0} \\ \boldsymbol{0} & \dot{\boldsymbol{C}}_2 & \boldsymbol{0} & \boldsymbol{0} & \boldsymbol{C}_2 & \boldsymbol{0} \\ \boldsymbol{0} & \boldsymbol{0} & \dot{\boldsymbol{C}}_3 & \boldsymbol{0} & \boldsymbol{0} & \boldsymbol{C}_3 \\ \dot{\boldsymbol{C}}_2 & \dot{\boldsymbol{C}}_1 & \boldsymbol{0} & \boldsymbol{C}_2 & \boldsymbol{C}_1 & \boldsymbol{0} \\ \dot{\boldsymbol{C}}_3 & \boldsymbol{0} & \dot{\boldsymbol{C}}_1 & \boldsymbol{C}_3 & \boldsymbol{0} & \boldsymbol{C}_1 \\ \boldsymbol{0} & \dot{\boldsymbol{C}}_3 & \dot{\boldsymbol{C}}_2 & \boldsymbol{0} & \boldsymbol{C}_3 & \boldsymbol{C}_2 \end{bmatrix} \tag{3.34}$$

where in practice, (3.34) is evaluated using the latest estimated DCM states.

3.3 Quaternion Formulation

3.3.1 Quaternion States

A rotation quaternion is be defined as

$$q = q_0 + \boldsymbol{q} = q_0 + q_1\boldsymbol{i} + q_2\boldsymbol{j} + q_3\boldsymbol{k} \qquad (3.35)$$

with the four parameters (q_0, q_1, q_2, q_3). This has been the most preferable formulation of the attitude in the inertial navigation algorithm so far. The time derivatives of these four parameters are used to model the change of a system's attitude. Here, a total of 8 attitude states are chosen. Accordingly, the attitude matrix from the navigation frame to the body frame is expressed as follows [Zhang and Sun, 1992]

$$\boldsymbol{C_n^b} = (q_0^2 - |\boldsymbol{q}|^2)\boldsymbol{I_3} - 2q_0[\boldsymbol{q}] + 2\boldsymbol{q}\boldsymbol{q^T} \qquad (3.36)$$

The subvector that describes the attitude states for the quaternion model is expressed as

$$\boldsymbol{x_a} = [q_0 \quad \boldsymbol{q^T} \quad \dot{q}_0 \quad \boldsymbol{\dot{q}^T}]^T \qquad (3.37)$$

Applying the same principles here as in Sections 3.1 and 3.2, the quaternion attitude states are considered to change linearly with time, accompanied by process noise defined by their second order time-derivatives. The kinematic model governing this attitude model is therefore given as follows

$$q_i(k+1) = q_i(k) + \dot{q}_i(k)\Delta t_{k+1} \quad i \in (0,1,2,3) \qquad (3.38)$$

with an associated transition matrix of

$$\mathbf{A}_a = \begin{bmatrix} \boldsymbol{I_4} & \Delta t_{k+1}\boldsymbol{I_4} \\ \boldsymbol{0_4} & \boldsymbol{I_4} \end{bmatrix} \qquad (3.39)$$

and an associated $\boldsymbol{\Gamma}$ matrix of

$$\mathbf{B}_a = \begin{bmatrix} \frac{1}{2}\Delta t_{k+1}^2\boldsymbol{I_4} \\ \Delta t_{k+1}\boldsymbol{I_4} \end{bmatrix} \qquad (3.40)$$

The connection between the attitude and the change of the quaternion vector is given via the Poisson Equation in (3.16)

$$\dot{q} = \frac{1}{2}\begin{bmatrix} q_0 & -q_1 & -q_2 & -q_3 \\ q_1 & q_0 & -q_3 & q_2 \\ q_2 & q_3 & q_0 & -q_1 \\ q_3 & -q_2 & q_1 & q_0 \end{bmatrix}\begin{bmatrix} 0 \\ \boldsymbol{\omega_{nb}^b} \end{bmatrix} \qquad (3.41)$$

from which $\boldsymbol{\omega_{nb}^b}$ is explicitly expressed as follows

$$\boldsymbol{\omega_{nb}^b} = 2\begin{bmatrix} -q_1 & q_0 & q_3 & -q_2 \\ -q_2 & -q_3 & q_0 & q_1 \\ -q_3 & q_2 & -q_1 & q_0 \end{bmatrix}\dot{q} = 2\boldsymbol{W}(q)\dot{q} \qquad (3.42)$$

Substituting (3.42) into (2.11) yields the following design submatrix

$$\boldsymbol{C_{g,a}} = \begin{bmatrix} \boldsymbol{0_{1,4}} & \boldsymbol{-2q_1} & \boldsymbol{2q_0} & \boldsymbol{2q_3} & \boldsymbol{-2q_2} \\ \boldsymbol{0_{1,4}} & \boldsymbol{-2q_2} & \boldsymbol{-2q_3} & \boldsymbol{2q_0} & \boldsymbol{2q_1} \\ \boldsymbol{0_{1,4}} & \boldsymbol{-2q_3} & \boldsymbol{2q_2} & \boldsymbol{-2q_1} & \boldsymbol{2q_0} \end{bmatrix} \qquad (3.43)$$

The accelerometer observation equations remain unchanged as in the derivation of (3.10), but the corresponding sub design matrix must be redefined for the quaternion states using the partial derivatives of the attitude matrix with respect to each of its elements:

$$\frac{\partial \boldsymbol{C_n^b}}{\partial q_0} = 2q_0\boldsymbol{I_3} - 2[\boldsymbol{q}] \qquad (3.44)$$

$$\frac{\partial \boldsymbol{C_n^b}}{\partial q_1} = -2q_1\boldsymbol{I_3} - 2q_0\begin{bmatrix} 0 & 0 & 0 \\ 0 & 0 & -1 \\ 0 & 1 & 0 \end{bmatrix} + 2\begin{bmatrix} 2q_1 & q_2 & q_3 \\ q_2 & 0 & 0 \\ q_3 & 0 & 0 \end{bmatrix} \qquad (3.45)$$

$$\frac{\partial \boldsymbol{C_n^b}}{\partial q_2} = -2q_2\boldsymbol{I_3} - 2q_0\begin{bmatrix} 0 & 0 & 1 \\ 0 & 0 & 0 \\ -1 & 0 & 0 \end{bmatrix} + 2\begin{bmatrix} 0 & q_1 & 0 \\ q_1 & 2q_2 & q_3 \\ 0 & q_3 & 0 \end{bmatrix} \qquad (3.46)$$

$$\frac{\partial \boldsymbol{C_n^b}}{\partial q_3} = -2q_3\boldsymbol{I_3} - 2q_0\begin{bmatrix} 0 & -1 & 0 \\ 1 & 0 & 0 \\ 0 & 0 & 0 \end{bmatrix} + 2\begin{bmatrix} 0 & 0 & q_1 \\ 0 & 0 & q_2 \\ q_1 & q_2 & 2q_3 \end{bmatrix} \qquad (3.47)$$

Using the partial derivatives defined from (3.44) to (3.47), the portion of the design matrix for the accelerometer measurements that refers to the attitude parameters may be redefined as

$$\boldsymbol{C_{s,a}} = \begin{bmatrix} \frac{\partial \boldsymbol{C_n^b}}{\partial q_0}\boldsymbol{s} & \frac{\partial \boldsymbol{C_n^b}}{\partial q_1}\boldsymbol{s} & \frac{\partial \boldsymbol{C_n^b}}{\partial q_2}\boldsymbol{s} & \frac{\partial \boldsymbol{C_n^b}}{\partial q_3}\boldsymbol{s} & \boldsymbol{0_4} \end{bmatrix} \qquad (3.48)$$

3.3.2 Quaternion State Constraints

The use of 8 quaternion states implies 2 redundant states, which require 2 state constraints to overcome the over-parameterization issue.

The first quaternion state constraint comes from the definition of a rotation quaternion:

$$qq^* = q_0^2 + |\boldsymbol{q}|^2 = 1 \qquad (3.49)$$

Moreover, as (3.49) should remain constant through time, its time first order derivative should be equal to 0, which yields the second constraint on the change of the quaternion:

$$q_0\dot{q}_0 + q_1\dot{q}_1 + q_2\dot{q}_2 + q_3\dot{q}_3 = 0 \qquad (3.50)$$

After their linearization, the coefficient matrix of the linearized constraints is as

$$\boldsymbol{H}_{\boldsymbol{q},\boldsymbol{a}} = \begin{bmatrix} 2q_0 & 2q_1 & 2q_2 & 2q_3 \\ \dot{q}_0 & \dot{q}_1 & \dot{q}_2 & \dot{q}_3 \\ 0 & 0 & 0 & 0 \\ q_0 & q_1 & q_2 & q_3 \end{bmatrix} \quad (3.51)$$

where in practice, (3.51) is realized using the most recently estimated quaternion states.

4. COMPREHENSIVE ERROR ANALYSIS

To estimate the residuals of the process noise and observation vectors the framework of the system state-constrained KF is applied [Wang et al, 2022].

The update of the state vector using the nonlinear constraints from Sections 3.2.2 and 3.3.2 is as follows [Wang et al, 2022]:

$$\boldsymbol{x_h}(k+1) = \boldsymbol{x}(k+1) - \\ -\boldsymbol{D_{xx}}(k+1)\boldsymbol{H}(k+1)\big(\boldsymbol{H}(k+1)\boldsymbol{D_{xx}}(k+1)\boldsymbol{H^T}(k+1)\big)^{-1} \\ \Big(\boldsymbol{H}\big(\boldsymbol{x}(k|k)\big) - \boldsymbol{h}(k+1)\Big) \quad (4.2)$$

where $\boldsymbol{x_h}(k+1)$ denotes the constrained KF solution at time t_{k+1}, and $\boldsymbol{D_{xx}}(k+1)$ denotes the covariance matrix for the unconstrained solution at time t_{k+1}.

The framework of the EKF formulation in [Wang et al, 2022] allows for the additional calculation of constrained system state, process noise, and observation residual vectors, as

$$\boldsymbol{v_h^x} = \boldsymbol{v^x} - \\ \mathbf{A}\boldsymbol{D_{xx}}\boldsymbol{\Phi^T}(\boldsymbol{I}-\boldsymbol{GC})^{\boldsymbol{T}}\boldsymbol{H^T}(\boldsymbol{HD_{xx}H^T})^{-1}\boldsymbol{h} \quad (4.3)$$

$$\boldsymbol{v_h^w} = \boldsymbol{v^w} - \\ \boldsymbol{Q}\mathbf{B}^{\boldsymbol{T}}(\boldsymbol{I}-\boldsymbol{GC})^{\boldsymbol{T}}\boldsymbol{H^T}(\boldsymbol{HD_{xx}H^T})^{-1}\boldsymbol{h} \quad (4.4)$$

and

$$\boldsymbol{v_h^z} = \boldsymbol{v^z} - \boldsymbol{CD_{xx}H^T}(\boldsymbol{HD_{xx}H^T})^{-1}\boldsymbol{h} \quad (4.5)$$

where $\boldsymbol{v_c^x}$, $\boldsymbol{v_c^w}$, and $\boldsymbol{v_c^z}$ are the residual vectors corresponding to the predicted system state, the process noise and observation vectors after the constraints are applied, respectively; $\boldsymbol{G}$ denotes the Kalman Gain matrix; $\boldsymbol{Q}$ denotes the covariance matrix for the process noise vector; and $\boldsymbol{h}$ is the misclosure of the constraint equations.

As our focus is on using these quantities to characterize performance of different attitude models, it is important to clarify several things with respect to their meaning and significance. Each of these residual vectors represent one of the three independent sources of error in a Kalman Filter at a specific time instant: estimated error in the measurements (observation residuals); estimated error in the kinematic models (process noise residuals); and error in the predicted system state vector (impacted by all the accumulated errors from the past). The residual vectors in (4.3), (4.4) and (4.5) are least-squares estimates and are statistically independent from one epoch to the next.

Since changing the attitude model primarily affects the system and measurement models, the performance of the process noise and observation residuals for each attitude model are particularly informative of each model's performance subject to our GMIS [Wang et al, 2015; Qian et al, 2015]. The EKF framework for comprehensive error analysis [Wang, 1997, 2008, 2009; Wang et al, 2022] is very well-suited for such analysis.

It is quite common to analyse the residuals of the double-differenced GNSS measurements. Unique to this research, the residuals of the raw IMU measurement vector and the system process noise vector are made available under the combination of our GMIS with the framework for comprehensive error analysis in KF. Particularly, the residuals of the gyro and accelerometer measurements are more indicative of the performance of each attitude model when drawing comparisons due to their connection to the system attitude. Similarly, the process noise residual vector has components that refer to the system jerk vector (i.e. third order time-derivative of the position vector) and the second time-derivative of the system's attitude-related states. The latter is more directly indicative of the system models associated with each attitude model.

Of particular importance is that the residual vectors could be used to conduct Variance Component Estimation (VCE). This involves taking the quadratic form $\boldsymbol{v_i^T D_{v_i v_i}^{-1} v_i}$ for a set of residual values and normalizing by their contribution to the overall degrees of freedom (DOF) of the Kalman Filter system. This DOF contribution is calculated [Forstner, 1979; Wang, 2009] as follows

$$DOF_i = \mathrm{tr}\big(\boldsymbol{D_{v_i v_i}}\boldsymbol{D_{l_i l_i}^{-1}}\big) \quad (4.6)$$

where $\boldsymbol{D_{v_i v_i}}$ denotes the covariance matrix for the residual vector $\boldsymbol{v_i}$ a variance factor is being calculated for, and $\boldsymbol{D_{l_i l_i}}$ denotes the *a priori* covariance matrix for the corresponding the observation vector $\boldsymbol{l_i}$.

Generally, the estimated variance components provide information for improving the *a priori* stochastic model based on the posteriori residuals and the redundancy contribution of measurements in Kalman filtering. In practice, this extends to all three independent error sources in the KF, and it is desirable to define subsets of the residual vectors so as to provide the most meaningful results with VCE. In this paper, the focus is primarily on the process noise/observation variance components, with the following sets of variance components calculated:
For the process noise residuals:

a. An overall variance component accounting for the entire process noise vector, which is used to provide an overall overview of the performance of the system model in Kalman filtering; and
b. Separate variance components accounting for all orientation-related elements and all position-related elements in the process noise vector. This may provide more granular information about the performance of each specific part of the system model.

For the measurement residuals:

a. An overall variance component accounting for the entire observation vector. This provides information about the overall performance of the measurement models from each attitude model being used.
b. Separate variance components dedicated to characterizing the performance of the raw gyroscope and accelerometer measurements. This is an essential innovation achieved by the combination of our GMIS with the framework of comprehensive error analysis in Kalman filtering as it is not feasible in the existing traditional inertial-aided integrated navigation.
c. A variance component accounting for the GNSS-related DD observation vector. Moreover, the variance of unit weight for each of L1 C/A, L1 Carrier Phase and L2 Carrier Phase measurements.

One limitation that is important to take into account when conducting VCE for a KF application is in the overall DOF for each subset of the residual vectors. Generally, a KF has a total DOF that is equal to the number of observations recorded plus the number of system state constraints at an epoch. The sum of the DOF contributions of the system state vector, process noise vector, and observation vector yields the overall DOF of the system for any given epoch. These redundancy contributions are not distributed uniformly among these (pseudo) observation elements. In VCE, a significantly small DOF (i.e., the redundancy index) may lead to an unreliable estimate of the associated variance component, as the estimated process noise typically comes with a low redundancy contribution [Wang et al, 2009]. This necessitates estimating variance components over a time interval, rather than epoch-wise, thereby increasing the reliability of the variance component. At the same time, conducting VCE over a specified time interval may reduce its time-domain resolution. Practically speaking, epoch-wise residuals reflect more identifiable "spikes" when there are problems in the system model and/or measurements.

5. COMPARATIVE ANALYSIS

5.1 General Attitude Model Performance

This section presents the results from a fifteen-minute-long kinematic dataset collected from a land vehicle equipped with our in-house developed integrated navigation system with an IMU 440 sensor operating at 100 Hz and a NovAtel OEM4 receiver operating at 1 Hz while a second NovAtel receiver was operated at a fixed location as a base station. The *a priori* standard deviation of the accelerometers was 0.1 m/s^2, and the *a priori* standard deviation of the gyros was 0.8 °/s. The vehicle stayed in stationary for the first 7.5 minutes and was then driven in kinematic for another 7.5 minutes. The horizontal trajectory of the land vehicle is shown in Fig. 5.1, and the velocity and acceleration profiles are shown in Fig. 5.2 and 5.3, respectively.

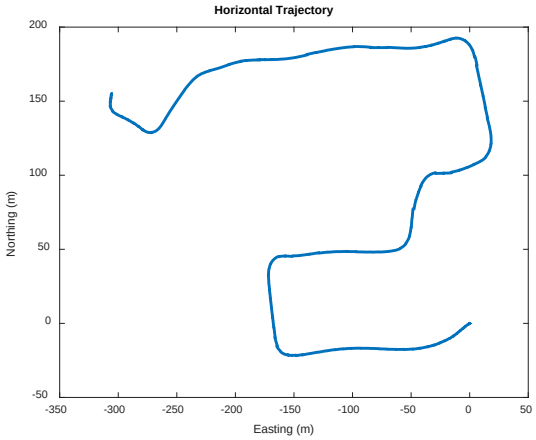

Fig. 5.1: Horizontal trajectory of the kinematic dataset used in this research. Note that coordinates are local geodetic coordinates relative to the starting location

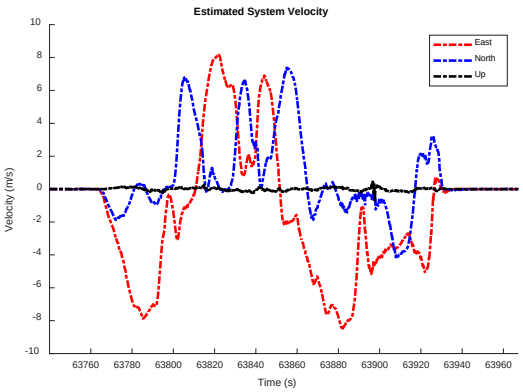

Fig. 5.2: System velocity profile of the kinematic dataset. Velocities expressed in the navigation frame local geodetic coordinates.

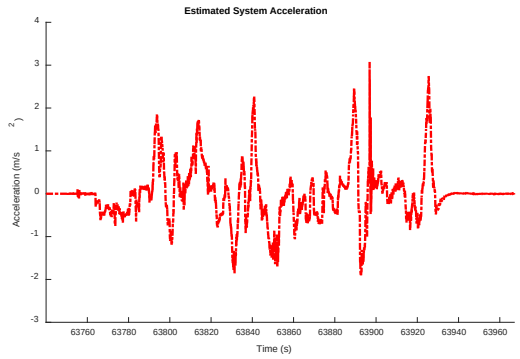

Fig. 5.3: System acceleration profile for the kinematic dataset. Accelerations expressed in the navigation frame local geodetic coordinates.

After the GMIS, each of the three proposed attitude models was implemented to process the test data. Then, comprehensive error analysis was directly applied to compare their solution performance. Specifically, the comparison is focused on:

1) Direct comparison of the state estimates. This is realized through the RMSE between different position/attitude estimates to provide a sense of consistency between the three different attitude models.
2) Direct comparison of the posteriori residuals and also the posteriori variance components to provide insight into the accuracy of each solution, and characterize the differences through the error behaviors in the system model and measurements while using different attitude models.

A summary of the RMSE between the kinematic portion of the position estimates using each attitude model is provided in Table 1. For the Roll-Pitch-Heading (RPH) model, the average standard deviation estimated for the position was 4.48 cm in the horizontal and 6.69 cm in the vertical; for the DCM model, the average estimated position standard deviation was 4.65 cm in the horizontal and 6.91 cm in the vertical; for the quaternion model, the average estimated position was 4.76 cm in the horizontal and 6.86 cm in the vertical. The estimated RMSE values between the different solutions are consistent with these estimated standard deviations.

Tab. 1: RMSE between the 3D positioning estimates for each attitude model, in cm. These values were calculated using only the kinematic portion of the dataset.

	RPH	DCM	Quaternion
RPH	0	4.57	3.84
DCM		0	3.95
Quaternion			0

A summary of the RMSE between the kinematic portion of the attitude estimates using each attitude model is provided in Table 2. To realize this analysis, the DCM and quaternion solutions were converted to their equivalent RPH representation to directly compare the attitude estimates. For the RPH model, the average standard deviation for the attitude was 0.11° in the roll and pitch and 0.34° in the heading; for the DCM model, the average estimated attitude standard deviation was 0.12° in the roll and pitch and 0.36° in the heading; for the quaternion model, the average estimated attitude standard deviation was 0.11° in the roll and pitch and 0.32 ° in the heading. The estimated RMSE values between the different solutions are consistent with these estimated standard deviations.

Tab. 2: RMSE between the attitude estimates for each attitude model [arcmin]. These values were calculated by converting to the equivalent RPH representation for the kinematic portion of each dataset.

	RPH	DCM	Quaternion
RPH	0	21.8	21.2
DCM		0	28.3
Quaternion			0

The RMSE between different attitude models suggests that these attitude models may be used interchangeably, disregarding software efficiency needs and degenerate cases (i.e. Gimbal Lock).

Analysing RMSE values between the three different attitude models is important when characterizing their performance to establish consistency between the models. Additional information may be gleaned from the estimated variance components when using each attitude model.

The variance components were estimated using the residuals of the observation and process noise vectors. The measurement residuals are shown in Fig. 5.4 for the three gyros' measurements, Fig. 5.5 for three accelerometers, Fig. 5.6, Fig. 5.7 and Fig. 5.8 show the measurement residuals for the GPS L1 C/A, L1 carrier phase and L2 carrier phase measurements, respectively.

Again, the IMU measurement residuals in Fig. 5.4 and 5.5 are only possible through using the GMIS, and would not be possible to estimate under the traditional integration strategy. These residuals are necessary to estimate any observation variance components, which is central to this comparative analysis. The histograms of each standardized set of residuals corresponding to individual measurements are shown in Fig. 5.9 to 5.13.

As can be seen from the histograms, all of these residuals appear reasonably well-behaved as random errors, which suggests that each of the attitude models is valid and performing well over the dataset.

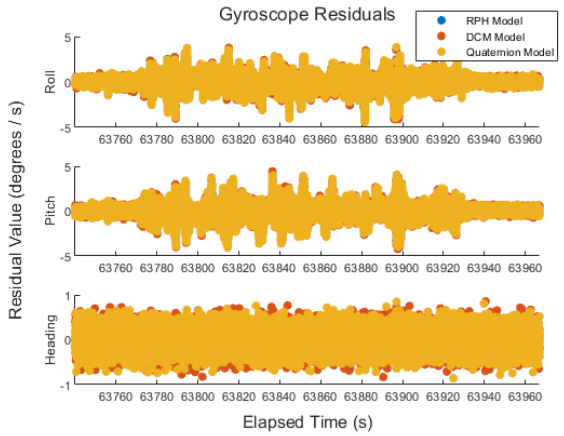

Fig. 5.4: Gyroscope residuals for each attitude model.

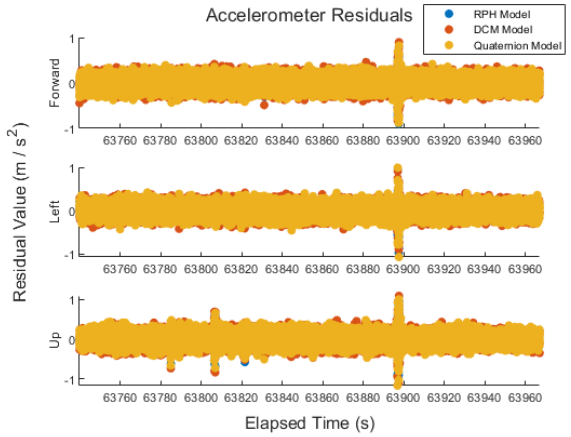

Fig. 5.5: Accelerometer residuals for each attitude model.

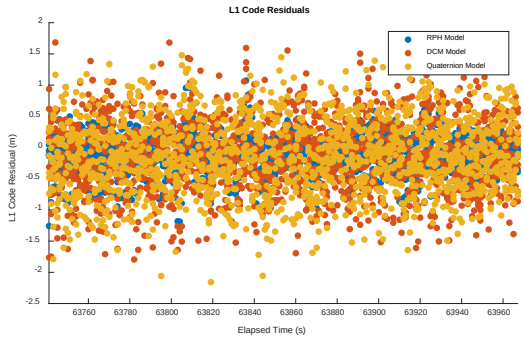

Fig. 5.6: L1 code residuals for each attitude model.

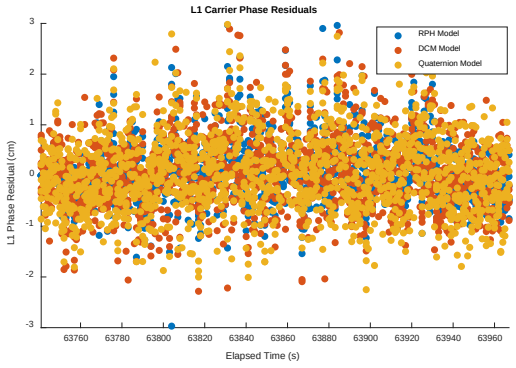

Fig. 5.7: L1 carrier phase residuals for each attitude model.

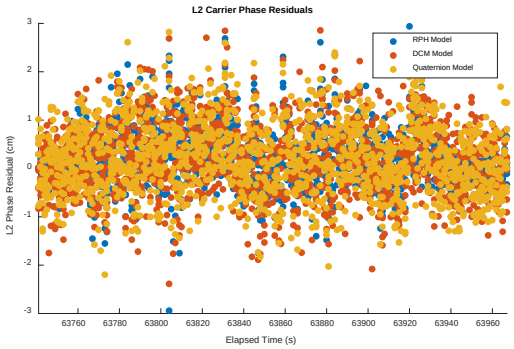

Fig. 5.8: L2 carrier phase residuals for each attitude model.

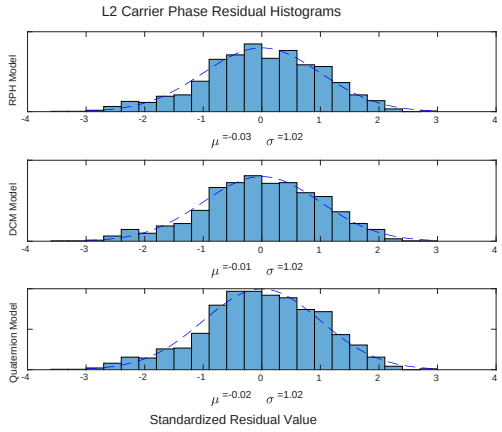

Fig. 5.9: Histogram of L1 C/A standardized residuals. Standard normal distribution superimposed for reference.

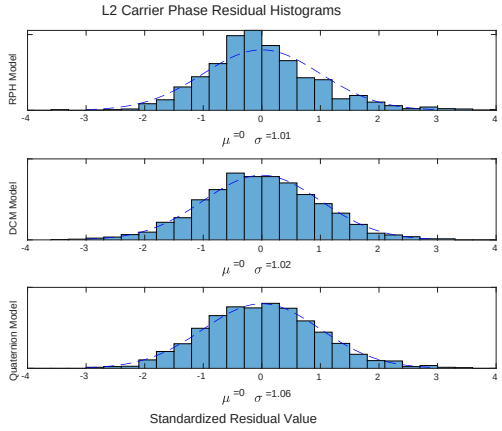

Fig. 5.10: Histogram of L1 carrier phase standardized residuals. Standard normal distribution superimposed for reference.

There are noticeable spikes near zero in both the gyroscope and accelerometer residual histograms in Fig. 5.12 and 5.13. These are largely from portions of the dataset where the system was moving with near-constant velocity.

The components of the process noise residual vector are shown in Fig. 5.14 and 5.15, with their associated histograms shown from Fig. 5.16 to 5.19. In general, the residuals of the jerk vector (Fig. 5.14 and 16) appear to behave quite well for all three models, as

do the residuals of the attitude process noise vector in Fig. 5.15, and 17 - 19.

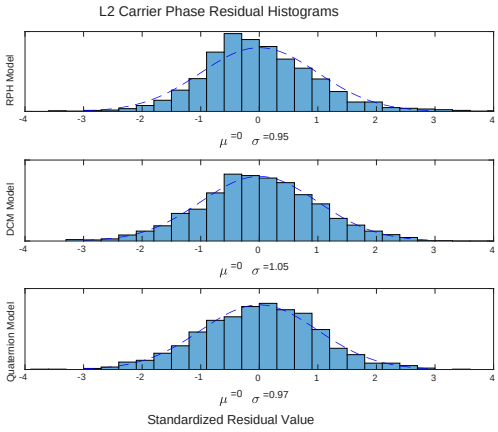

Fig. 5.11: Histogram of L2 carrier phase standardized residuals. Standard normal distribution superimposed for reference.

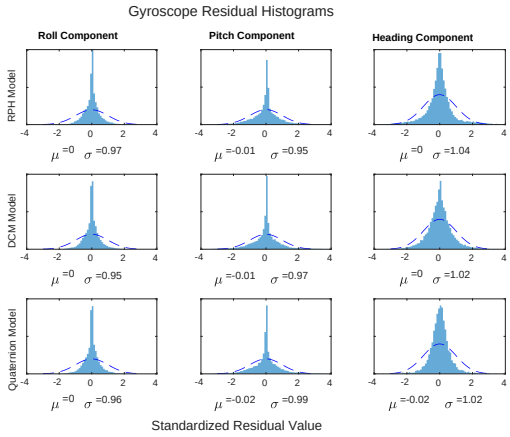

Fig. 5.12: Histograms of gyroscope standardized residuals. Standard normal distribution superimposed for reference.

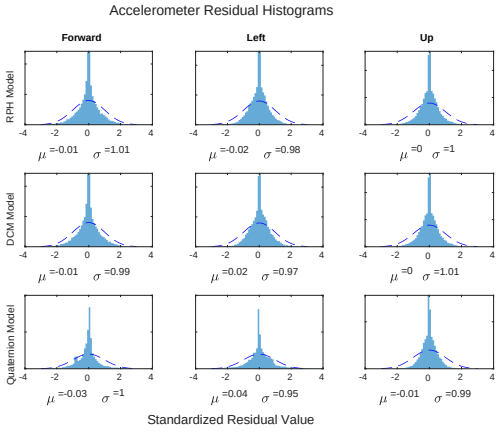

Fig. 5.13: Histogram of accelerometer standardized residuals. Standard normal distribution superimposed for reference.

As was the case with the IMU measurement residual histograms, the system jerk histograms in Fig. 5.16 exhibit strong spikes near zero, which again coincides with times when the system was moving at a near-constant velocity. In general, it is reasonable to expect process noise to have different stochastic properties under different dynamic conditions.

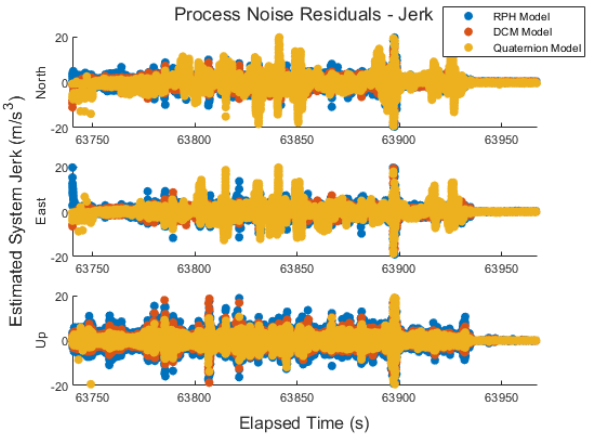

Fig. 5.14: Residuals of system jerks (process noises).

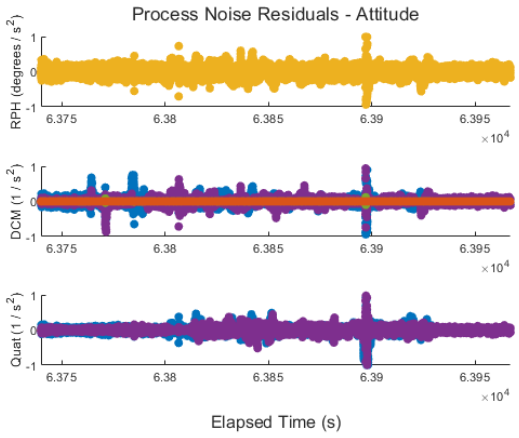

Fig. 5.15: Estimated process noise residuals for the attitude parameters. Each colour represents a different second-order time derivative of a different parameter in the associated attitude model.

From the histograms in Fig. 5.17 to 5.19, it is clear that the process noise estimates for attitude parameters related to the system heading have a much broader range of values than for other attitude parameters not related to the system heading. This is due to the fact that the dataset was collected from a land vehicle, and the pitch/roll of the system did not change much over the course of the entire kinematic dataset. For example, change in system heading may be represented as a rotation about the z-axis for an approximately level vehicle. Elements C_{11}, C_{12}, C_{21}, and C_{22} of the DCM model all change significantly with rotation about the z-axis, but the other attitude parameters do not change significantly. Similarly, q_0 varies with the overall angle of rotation and q_3 varies with rotation about the z-axis, but q_1 and q_2 do not change significantly as the heading changes.

All variance factors (their individual variances of unit weight) were regionally estimated over a moving

time period of 20 seconds. This time period could be increased to provide a more accurate sense of overall performance for each variance component or decreased to provide a more precise estimate of when issues in the positioning solution arise. All plots display the standard error, which is the square root of the estimated variance of unit weight.

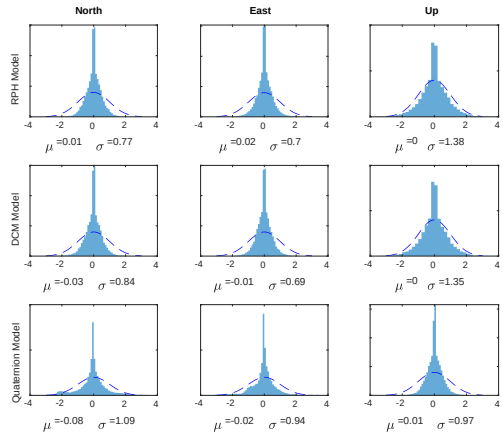

Fig. 5.16: Histogram of system jerk process noise residuals.

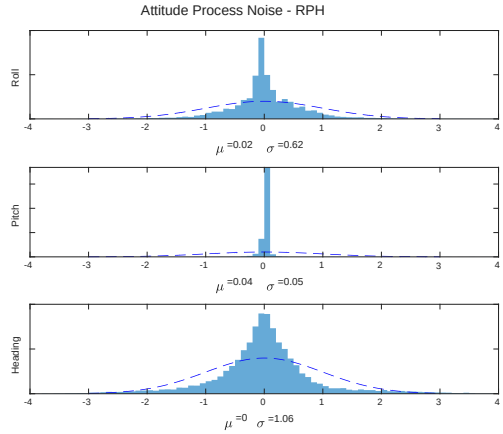

Fig. 5.17: Histogram of attitude process noise for the RPH attitude model.

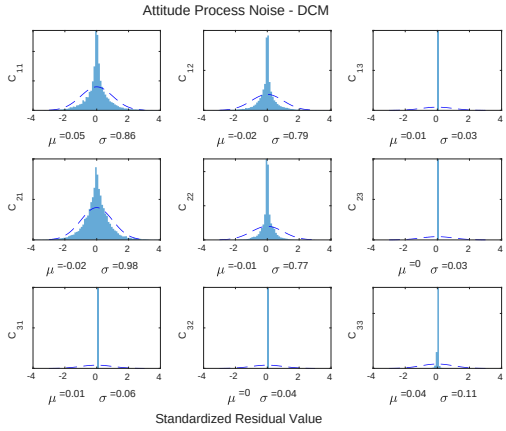

Fig. 5.18: Histogram of attitude process noise for the DCM attitude model.

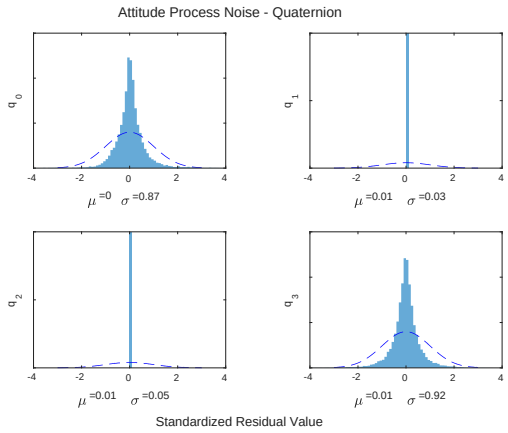

Fig. 5.19: Histogram of attitude process noise for the quaternion attitude model.

The overall global *posteriori* observation standard error plots are shown in Fig. 5.20, and the estimated overall process noise standard error plots are shown in Fig. 5.21.

The estimated standard error for both observations and process noise are very consistent between the different attitude models. These plots feature much lower values towards the beginning and the end of the dataset, when the positioning system was stationary. This is to be expected for the process noise since the process noise represents the higher-order motion of the system, which should be zero for a stationary system. It also makes sense for the observations, since their quality when stationary is not confounded by systematic errors from the system's motion (for example, vibration of the sensors).

Overall, the shape of each plot in Fig. 5.14 and 5.15 are very similar; the positioning/orientation KF responds similarly for each attitude model, with only relatively minor discrepancies between their estimated standard errors.

The average estimated observation standard errors associated with each attitude model are summarized in Table 3. This table includes the overall estimated standard error components for IMU gyro, IMU accelerometer, and GPS observations. Table 4 shows both the *a priori* and *a posteriori* estimates of each observation type's accuracy for each attitude model. All attitude models used the same *a priori* estimates of the observation accuracy.

Overall, the posteriori standard errors are very consistent between different attitude models (Table 4). All observation standard error components of unit weight converge to approximately 1 (Table 3), which indicates that observation accuracies were properly tuned and that there are no issues in the relative weighting between different observation types.

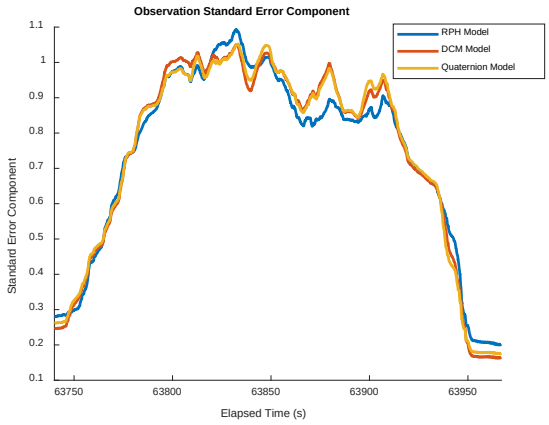

Fig. 5.20: The standard error plots for the observation residual vector in the RPH, DCM, and Quaternion attitude models (moving window: 20s)

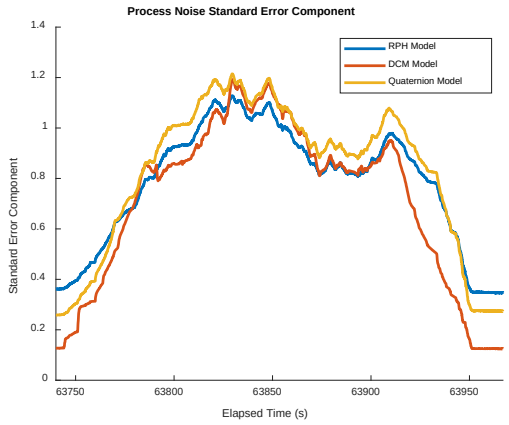

Fig. 5.21: The standard error plots for the process noise residual vector in each attitude model (moving window: 20s)

Tab. 3: Overall estimated standard errors of unit weight for each type of measurements, and for all observations together associated with each of the attitude models. Each standard error of unit weight was evaluated solely over the mobile period of the dataset.

	Standard Errors of Unit Weight ($\hat{\sigma}_0$)					
Attitude Model	**Accelerometer**	**Gyroscope**	**L1 C/A**	**Carrier Phase**		**Overall**
				L1	**L2**	
RPH	1.0154	1.0132	1.0255	1.0236	0.9955	1.0026
DCM	0.9613	1.0097	1.0256	1.0512	1.0032	0.9966
Quaternion	0.9646	0.9921	1.0254	1.0601	0.9648	0.9789

Tab. 4: Overall estimated a priori and a posteriori standard deviations for each type of measurement. A posteriori standard deviations were estimated by scaling the a priori standard deviation estimate by the standard error of unit weight provided in Table 3.

	***A Posteriori* Standard Deviations**				
	Accelerometer [m/s^2]	**Gyroscope [^{o}/s]**	**L1 C/A [m]**	**Carrier Phase [cm]**	
				L1	**L2**
RPH	0.102	0.811	0.513	0.512	0.498
DCM	0.096	0.808	0.513	0.526	0.502
Quaternion	0.096	0.794	0.513	0.530	0.482

Comparing the absolute *a posteriori* standard deviations of each observation type for each attitude model in Table 4 makes it clear that they are very compatible with one another.

The global posteriori process noise standard errors of unit weight for each attitude model are summarized in Table 5. This table includes the average estimated variance components for the system jerk (i.e. third-order linear motion) and the second time-derivatives of the attitude parameters. Table 6 shows the *a priori* and *a posteriori* estimates of the accuracies of the position and attitude process noise components.

As with the observation variance components, the estimated standard error components for the process noise elements converge to approximately 1. This suggests that the *a priori* estimates of the process noise components are consistent with their *a posteriori* estimates.

Tab. 5: Overall estimated standard errors of unit weight for each process noise component related to the motion in the system. Note that components related to the wander of IMU systematic errors and GPS ambiguity estimates (before fixed) are not included in this table, but did contribute to the overall process noise variance of unit weight estimate.

Attitude Model	Standard Errors of Unit Weight ($\hat{\sigma}_0$)		
	Jerk Vector	**Angular Acceleration Vector**	**Overall Process Noise Vector**
RPH	0.9231	0.9580	0.9718
DCM	0.8975	0.9216	0.9329
Quaternion	0.9012	0.9289	0.9826

Tab. 6: Overall estimated a posteriori estimates of the process noise jerk and angular acceleration components.

Attitude Model	Standard Deviations	
	Jerk [m/s^3]	**Angular Acceleration [°/s^2]**
RPH	9.231	0.958
DCM	8.975	0.922
Quaternion	9.012	0.929

As with the observation variance components, the estimated standard error components for the process noise elements converge to approximately 1. This suggests that the *a priori* estimates of the process noise components are consistent with their *a posteriori* estimates.

5.2 Response to System Jolt

To this point, the consistency between different attitude models has been established, and it appears that all three attitude models perform well under normal operating conditions. It is informative, however, to investigate how each attitude model responds to "stress," and how they cope with outlier measurements.

Upon investigation we discovered that for our dataset, the system was jolted at about the 63900 second mark as illustrated by the high rate IMU measurements (Fig. 5.22), and this jolt impacted IMU measurements for a duration of approximately 0.5 seconds. The results in Section 5.1 were all generated by flagging and removing the observations that were affected by the system jolt, but all results in this subsection purposefully use those observations to investigate the strain they place on the different attitude models.

The estimated overall observation standard error plots are shown in Fig. 5.23, the estimated gyroscope standard error plots are shown in Fig. 5.24, the estimated accelerometer standard error plots are shown in Fig. 5.25, and the estimated GPS observation standard error plots are shown from Fig. 5.26 to Fig. 5.28. Each plot shows the estimated standard error with a 20 second moving window for each attitude model, to better facilitate a direct comparison.

The system jolt is important to bear in mind in interpreting these plots, noting that the jolt primarily affected the IMU gyro measurements.

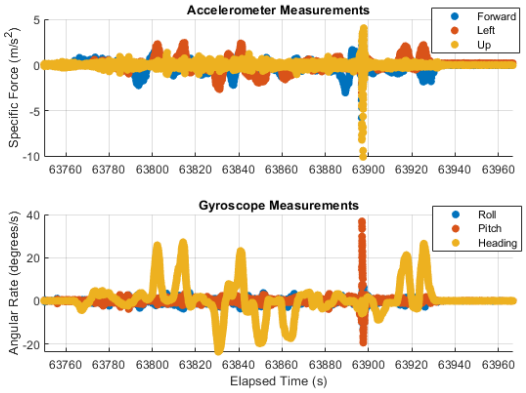

Fig. 5.22: IMU measurement plots over the duration of the mobile observation period. Note the sharp jumps at approximately t = 63897.

Looking at the estimated standard errors of unit weight over a 20s window from Fig. 5.23 to Fig. 5.28, the impact of the system jolt is quite apparent, as it produced a jump in all IMU standard error components near the 63900 second mark. It is important to note that the system jolt was almost instantaneous, but that the associated jump in standard error estimates occurs over a much longer period of time. This is due to the fact that the standard error components are evaluated over a time interval, rather than on an epoch-by-epoch basis. If the goal of VCE were to detect and remove these issues, rather than to characterize performance more broadly, evaluating variance components over a smaller time interval would improve the time-domain resolution. As illustration, Fig. 5.29 shows the estimated standard error of unit weight for the observation vector using a window size of 1 second. The standard errors of unit weight in 5.29 show a much more localized jump near the time of the system jolt,

but provides more noisy estimates of the standard error over the rest of the dataset.

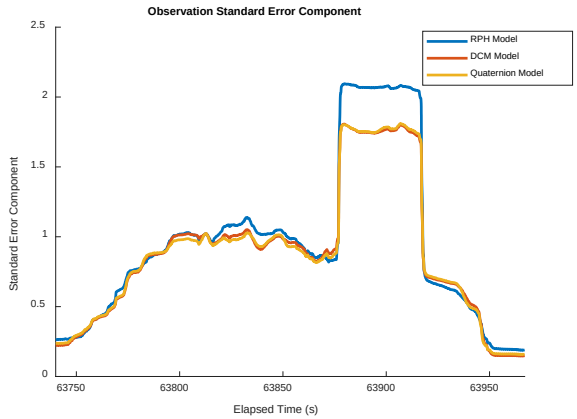

Fig. 5.23: Estimated observation standard errors of unit weight for each attitude model (moving window: 20s). Note the sharp jump in all models around the time 63900 seconds.

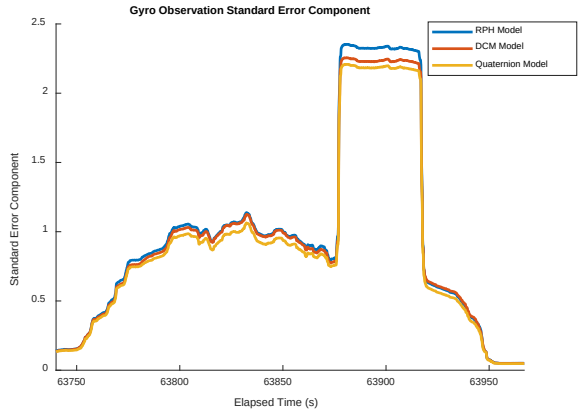

Fig. 5.24: Estimated gyro observation standard errors of unit weight for each attitude model (moving window: 20s).

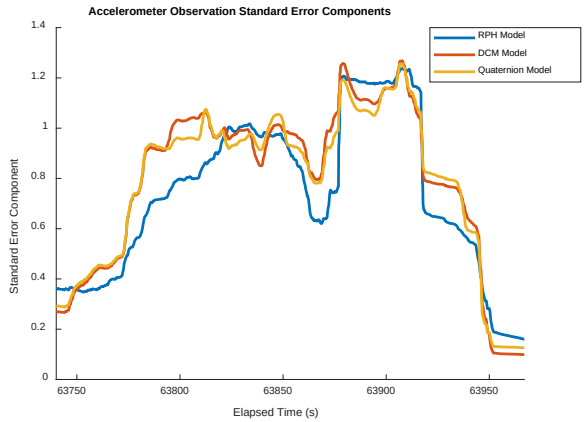

Fig. 5.25: Estimated accelerometer standard errors of unit weight for each attitude model (moving window: 20s).

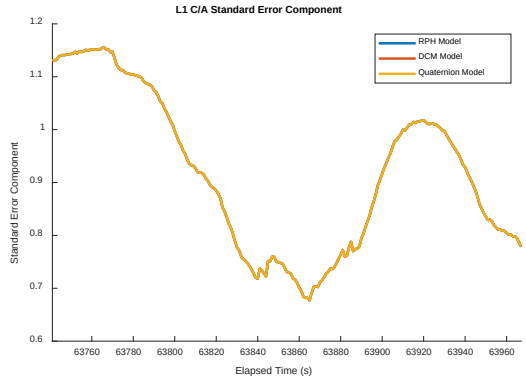

Fig. 5.26: Estimated L1 C/A standard errors of unit weight for each attitude model (moving window: 20s).

Of particular note in Fig. 5.23 and Fig. 5.24 is the fact that the system jolt affected standard error estimates very similarly across all attitude models. This suggests that each attitude model has a similar response to erroneous observations.

Additionally, the standard error estimates from Fig. 5.25 to 5.28 display a much less pronounced impact from the system jolt than for the overall/gyroscope standard error estimates. This suggests that using VCE in the GMIS allows users to reliably identify specific sensors that are degrading solution quality.

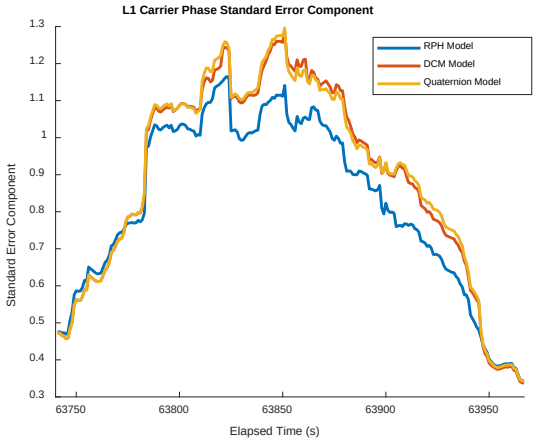

Fig. 5.27: Estimated L1 carrier phase standard errors of unit weight for each attitude model (moving window: 20s)

The estimated process noise standard errors of unit weight are shown in Fig. 5.30, the estimated system jerk standard error components are shown in Fig. 5.31, and the estimated second time-derivative of the attitude parameters' standard error components are shown in Fig. 5.32. As with the observation standard error components, each plot shows the estimated standard error components for each attitude model, to better facilitate a direct comparison between them.

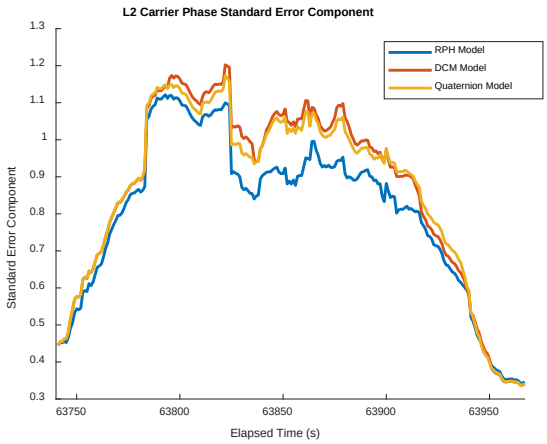

Fig. 5.28: Estimated L2 carrier phase standard errors of unit weight for each attitude model (moving window: 20s)

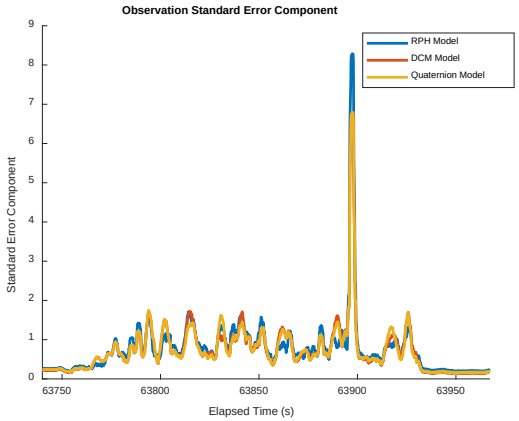

Fig. 5.29: Estimated standard errors of unit weight for the overall observation vector (moving window: 1s). Note that the "spike" from the system jolt is much more localized, but the overall standard error estimates are much noisier.

It is important to note that the plots shown include the standard error components related to the overall performance of the process noise residual vector, its components that are related to the system position, and its components that are related to the system attitude. There are more elements to the process noise residual vector than just those related to system position/attitude, including elements referring to the drift of IMU systematic errors and integer ambiguity estimates before they have been fixed. These elements of the process noise vector could be used to estimate associated standard error components, but such standard error components are considered not relevant for the purposes of this research.

The estimated standard errors of unit weight for the overall process noise vector (Fig. 5.30) appear to be dominated by the behaviour of the process noise standard error component for the second time-derivative of the attitude parameters (Fig. 5.32).

Overall, the behaviour of the process noise standard error components is very similar for all three attitude models. Each set of process noise standard error estimates appears to be influenced by the system jolt, particularly for the process noise elements related to the system attitude. It is particularly clear in Fig. 5.26 that the attitude process noise standard error estimates were most negatively impacted for the RPH model, with the Quaternion model having a smaller negative impact and the DCM model being the least impacted. Since all attitude models represent the angular motion of the system using the first-order derivatives of their attitude parameters, it is reasonable that they behave differently under different strains on the system.

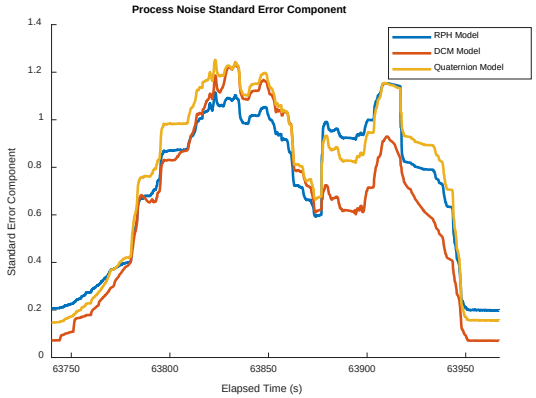

Fig. 5.30: Estimated process noise standard errors of unit weight for each attitude model (moving window: 20s).

In Fig. 5.31, the estimated standard errors of unit weight corresponding to the system jerk appear to exhibit largely similar behaviours across all different attitude models that were used. There was a jump associated with the system jolt for each attitude model, but these were a bit less pronounced than for the attitude parameters' second time-derivatives.

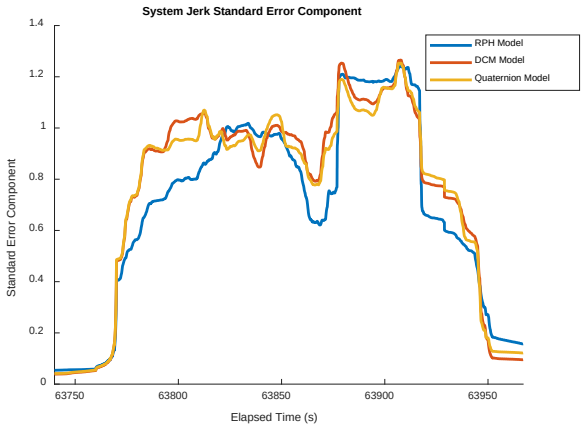

Fig. 5.31: Estimated system jerk standard errors of unit weight for each attitude model (moving window: 20s).

These results indicate that the DCM model is the most resistant to observation errors creeping into the KF system state prediction. This may be due to the larger number of constraints that the DCM model must adhere to, which might provide more strict limits on sudden

changes to attitude estimates for the DCM model. This, of course, comes with the caveat that the DCM model uses 18 attitude parameters, as opposed to the RPH model's 6 parameters and the Quaternion model's 8 parameters. It is important to note that this does not imply that the DCM model outperforms the others, but rather that each model internalizes erroneous observations in different ways.

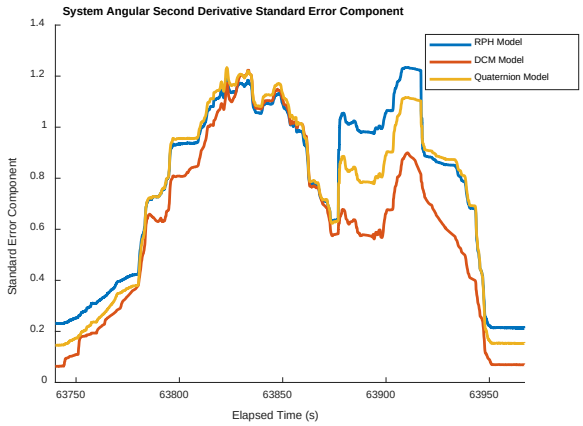

Fig. 5.32: Estimated standard errors of unit weight for the second time-derivative of the attitude parameters for each attitude model (moving window: 20s).

6. CONCLUDING REMARKS

The core purpose of this research is to extend attitude modeling in the GMIS to include the DCM and quaternion attitude models. To this end, the RPH, DCM, and quaternion attitude models were systematically studied. In traditional multisensor integration, the attitude dynamics are modeled directly via applying the IMU measurements in the free inertial navigation calculation, but this work instead predicts the attitude states using their time derivatives in their system model and then conducting the IMU measurement updates in EKF. Furthermore, this research is novel in formulating state constraint equations on both the attitude parameters and their first order time derivatives.

Moreover, the models developed for this research were fully realized and were successful in processing real road data, displaying strong capability in identifying specific elements that might degrade solution quality. The combination of the GMIS and comprehensive error analysis additionally allowed for a very thorough accounting for and analysis of system performance, and is very customizable in terms of what information is desired.

Tab. 7 provides an overview of the parameters governing the three attitude models used in this research. Generally, computational complexity increases with both the number of states being estimated and the number of constraints being applied, so the DCM and quaternion attitude models come with an additional computational cost compared to the RPH model. However, such computational burden seems not worrisome with using modern computers in comparison with the computing capability a few decades ago.

Tab. 7: Overview of each attitude model in the GMIS.

Attitude Model	No. of States	Number of Constraints	Process Noise
RPH	6	0	2nd Order
DCM	18	12	2nd Order
Quaternion	8	2	2nd Order

These models were directly linked to the IMU raw measurements, which allows for KF measurement updates when there is even only IMU data available. It also allows for direct estimation of residuals for the raw IMU (gyroscope and accelerometer) measurements, enabling much deeper system analysis, particularly in post-processing environments. Altogether, these contributions enabled a direct comparison to be made between different attitude models, without requiring either simulated data or a ground truth solution. This comparison demonstrated a general compatibility between the three attitude models used in this research outside of degenerate cases (i.e. Gimbal Lock), as well as a similar response to erroneous measurements.

Moreover, this work not only provided the complete algorithms of three attitude models, verified their equivalency and performance consistency within the scope of GMIS and also revealed the potential for multisensor data fusion at sensor level and for conducting comprehensive error analysis through the combination of the developed GMIS and comprehensive error analysis frame work in discrete Kalman filtering.

Acknowledgements

The authors greatly acknowledge the financial support from the Natural Sciences and Engineering Research Council of Canada (NSERC). They also thank Mr. Mike Ma at the Earth Observation Laboratory of York University for his help with the field work.

References:

Caspary, Wilhelm and Wang, Jianguo (1998): *Redundancy Contributions and Estimation of Variance Components in the Kalman Filter (German)*, No. 4, 1998, ZfV (Zeitschrift für Vermessung).

Choukroun, D., Weiss, H., Bar-Itzhack, I. Y., & Oshman, Y. (2010): Direction Cosine Matrix

Estimation from Vector Observations using a Matrix Kalman Filter, IEEE Transactions on Aerospace and Electronic Systems, 46(1).

Dreier, Ansgar, et al. "Quality Analysis of Direct Georeferencing in Aspects of Absolute Accuracy and Precision for a UAV-Based Laser Scanning System." *Remote Sensing*, vol. 13, no. 18, 18, Jan. 2021, p. 3564. *www.mdpi.com*, https://doi.org/10.3390/rs13183564.

Farrell, J. (1995): Integrated nav: the 2nd edition I never wrote, In: *Proc. of the 51st Annual Meeting* (*Colorado Springs CO. June* 5-7, 1995), pp. 443-446, The Inst. of Navigation, Alexandria V A.

Forstner, W. (1979): Ein Verfahren zur Schatzung von Varianz- und Kovarianzkomponenten, *Allgemeine Vermessungs-Nachrichten*, 1979.

Fresk, Emil, and George Nikolakopoulos (2013): FullQuaternion Based Attitude Control for a Quadrotor, *2013 European Control Conference (ECC)*, 2013, pp. 3864–69, *IEEE Xplore*.

Gołąbek, Michał, et al. "Quaternion Attitude Control System of Highly Maneuverable Aircraft." *Electronics*, vol. 11, no. 22, 22, Jan. 2022, p. 3775. *www.mdpi.com*, https://doi.org/10.3390/electronics11223775.

Hutton, Joe and Mohamed Mostafa (2005): 10 Years of direct Georeferencing for Airborne Photogrammetry, Photogrammetric Week 2005, Germany.

Meng, Z.; W. Ren and Z. You (2010): Decentralised cooperative attitude tracking using modified Rodriguez parameters based on relative attitude information, International Journal of Control, 83(12), 2427–2439.

Özgür Doruk, R. (2009): Linearization in satellite attitude control with modified Rodriguez parameters. Aircraft Engineering and Aerospace Technology, 81(3), 199–203.

Prasetyo, E.; Trihapningsari, D. and Musa, P. (2021): Comparative Performance Evaluation of Direction Cosine Matrix and Madgwick's as 3DOrientation Estimation Algorithm, ICIC Express Letters, 15, 409–420, 2021.

Qian, Kun (2017): Generic Multisensor Integration Strategy and Innovative Error Analysis for Integrated Navigation, PhD Dissertation, York University, 2017.

Qian, Kun; Wang, Jianguo and Hu, Baoxin (2016): A posteriori estimation of stochastic model for multisensor integrated inertial kinematic positioning and navigation on basis of variance component estimation, Journal of GPS, 2016, 14:5.

Qian, Kun; Wang, Jianguo and Hu, Baoxin (2015): Novel integration strategy for GNSS-aided inertial integrated navigation, Geomatica, 2015, No. 2, Vol. 69, pp. 217-230.

Sabatini, A. M. (2006): Quaternion-based extended Kalman filter for determining orientation by inertial and magnetic sensing. IEEE Transactions on Biomedical Engineering, 53(7), 1346–1356.

Salychev, Oleg S. (1998): Inertial Systems in Navigation and Geophysics, Bauman MSTU Press, Moscow, 1998.

Sheng, Hanlin and Tianhong Zhang (2015): MEMS Based Low-Cost Strap-down AHRS Research, *Measurement*, vol. 59, Jan. 2015, pp. 63–72.

Song, Jinlong, et al. "The Fast Attitude Estimation Method Based on Quaternion and Generalized Multivectors." *IEEE Transactions on Instrumentation and Measurement*, vol. 70, 2021, pp. 1–10. *IEEE Xplore*, https://doi.org/10.1109/TIM.2020.3018838.

Wang, J.; Brunson, B. and Hu, B. (2022): Innovative Formulation in Discrete Kalman Filtering with Constraints - A Generic Framework for Comprehensive Error Analysis, Journal of Global Positioning Systems, vol. 18, issue 1, 56–69.

Wang, Jianguo; Aaron Boda and Baoxin Hu (2021): Comprehensive error analysis beyond system innovations in Kalman filtering (Chapter 3), Book: Learning Control: Applications in Robotics and Complex Dynamical Systems, Edited by Dan Zhang and Bin Wei, Elsevier, 2021.

Wang, Jianguo; Kun Qian and Baoxin Hu (2015): An Unconventional Full Tightly-Coupled Multisensor Integration for Kinematic Positioning and Navigation, Lecture Notes in Electrical Engineering, China Satellite Navigation Conference (CSNC) 2015 Proceedings, Volume III, 2015, pp. 753–765.

Wang, Jianguo; Nilesh Gopaul and Bruno Scherzinger (2009): Simplified Algorithms of Variance Component Estimation for Static and Kinematic GPS Signle Point Positioning, Vol. 8, No. 1:43-51, Journal of Global Positioning Systems, 2009.

Wang, Jianguo (2009): Reliability Analysis in Kalman Filtering, Vol. 8, No. 1:86-96, Journal of Global Positioning Systems, 2009.

Wang, Jianguo (2008): *Test Statistics in Kalman Filtering*, Journal of Global Positioning Systems, Vol. 7, No.1, 2008, pp. 81~90.

Wang, Jianguo (1997): Filtering Methods for Error Tolerant Kinematic Positioning, PhD Diss., No. 52, Schriftenreihe Studiengang Vermessungswesen der Universität der Bundeswehr München, ISSN 0173-1009, Neubiberg, Germany, 1997.

Wang, L.-S., Chiang, Y.-T., & Chang, F.-R. (2002): Filtering method for nonlinear systems with constraints. IEE Proceedings – Control Theory and Applications, 149(6), 525–531.

Wang, Jianguo and Harald Sternberg (2000): Model Development for Kinematic Surveying of Land Vehicle Trajectories, No. 60-1, Schriftenreihe Studiengang Vermessungswesen der Universität der Bundeswehr Muenchen, pp. 317-331, ISSN 0173-1009, Neubiberg, Germany, 2000.

Wang, Y. and R. Rajamani (2018): Direction cosine matrix estimation with an inertial measurement unit, Mechanical Systems and Signal Processing, 109, 268–284.

Wagner, J. F. and T. Wieneke (2003): Integrating satellite and inertial navigation - conventional and new fusion approaches, Control Engineering Practice, 11(5), 543-550.

Yang, Y. (2012): Spacecraft attitude determination and control: Quaternion based method, Annual Reviews in Control, 36(2), 198–219.

Zhang, Shuxia and Jing Sun (1992): Strapdown Inertial Navigation Systems, textbook ((in Chinese), NationalDefense Press, 1992, Beijing.

Zhao, Long (2016): Modern Navigation Technologies, Lecture Slides, Graduate Course of Beijing University of Aeronautics and Astronautics, accessed in April 2023, dnc.buaa.edu.cn/info/1051/1433.htm.

Zhu, T.; Y. Liu; W. Li and K. Li (2021): The quaternion-based attitude error for the nonlinear error model of the INS. IEEE Sensors Journal, 21(22), 25782–25795.

Authors

Benjamin Brunson is currently a PhD student at York University. He obtained his Bachelor's Degree in Geomatics Engineering and MSc Degree in Earth and Space Science from the same university. His current research interests include data fusion for multisensor integrated kinematic positioning and statistical learning.

Jianguo Wang is a Professor in Geomatics Science and Engineering at the Department of Earth and Space Science and Engineering, York University, Canada. He holds a Dr.-Ing. in Surveying Engineering from the Universität der Bundeswehr München, Germany, a B.Eng. and a M. Eng. in Surveying Engineering from WTUSM (Wuhan Technical University of Surveying and Mapping. His current research interests include multisensor integrated kinematic positioning and navigation, optimal estimation methods, and data fusion, and statistical learning.